

# Production and dynamics of positrons in ultrahigh intensity laser-foil interactions

I. Yu. Kostyukov<sup>1, a)</sup> and E. N. Nerush<sup>1</sup>

*Institute of Applied Physics, Russian Academy of Science, 46 Uljanov str., 603950 Nizhny Novgorod, Russia*

The electron-positron pair production accompanying interaction of a circularly polarized laser pulse with a foil is studied for laser intensities higher than  $10^{24} \text{W cm}^{-2}$ . The laser energy penetrates into the foil due to the effect of the relativistic hole-boring. It is demonstrated that the electron-positron plasma is produced as a result of quantum-electrodynamical cascading in the field of the incident and reflected laser light in front of the foil. The incident and reflected laser light makes up the circularly polarized standing wave in the reference frame of the hole-boring front and the pair density peaks near the nodes and antinodes of the wave. A model based on the particle dynamics with radiation reaction effect near the magnetic nodes is developed. The model predictions are verified by 3D PIC-MC simulations.

## I. INTRODUCTION

Ultrahigh intensity laser-matter interaction attracts much attention, first of all, due to the fast development in laser technology<sup>1,2</sup>. At extremely high laser intensity the quantum-electrodynamical (QED) effects start to play a key role. Among them are: photon emission by electrons and positrons with strong recoil, photon decay in strong electromagnetic field with electron-positron pair creation (Breit-Wheeler process), Bethe-Heitler process, trident process, etc<sup>3,4</sup>. The laser-matter interaction in the QED-dominated regime leads to manifestation of new phenomena like prolific production of gamma-rays and electron-positron pairs<sup>5–11</sup>, laser-assisted QED cascading<sup>12–19</sup>, radiation trapping of the charged particles<sup>20–24</sup> etc.

In this paper we focus on laser-plasma interaction in the hole-boring (HB) regime when the light pressure pushes plasma inside the target<sup>25,26</sup>. The hole-boring front can be introduced as a plasma-vacuum interface propagating towards the target. The front separates the vacuum region from the high density plasma. The HB front structure is as follows. The laser pressure pushes the electrons ahead thereby forming the sheath with the unshielded ions and the thin, dense electron layer. Reflection and absorption of the laser light by the electron layer provides efficient laser pressure. The charge separation generates strong longitudinal electric field that, on the one hand, accelerates the ions towards the target and, on the other hand, suppress the electron acceleration by the laser pressure. Laser radiation and the plasma ions mostly contribute into the energy-momentum budget. The HB front velocity can be derived from the equation for the energy-momentum flux balance<sup>25,27,28</sup>

$$v_{HB} = \frac{c}{1 + \mu}, \quad (1)$$

where

$$\mu = \frac{1}{a_0} \sqrt{\frac{M n_i}{m n_{cr}}}, \quad (2)$$

$a_0 = eE/(mc\omega_L)$  is the normalized laser field strength,  $n_{cr} = m\omega_L^2/(4\pi e^2)$  is the critical plasma density,  $n_i$  is the density of the plasma ions,  $\omega_L$  is the laser frequency,  $M$  is the ion mass,  $c$  is the speed of light,  $m$  and  $e > 0$  are the electron charge and mass, respectively. It follows from Eqs. (1) and (2) that the HB front velocity increases with increasing of the laser intensity and decreasing of the plasma density. The electrons in the laser field can emit high energy photons and if the laser intensity is high enough then the portion of the laser energy converted into the gamma ray energy is large<sup>10</sup> so that the fluxes of the emitted gamma-photons has to be taken into account in the energy-momentum flux budget<sup>11</sup>. It is demonstrated<sup>11,29</sup> that the efficient generation of gamma-rays reduces the laser reflection and the HB front velocity.

Another effect accompanying the ultrahigh intensity laser-solid interaction is electron-positron pair creation<sup>6,7,11</sup>. The pairs can be created because of Breit-Wheeler process. Avalanche-like production of electron-positron pairs and gamma photons is possible at QED cascading<sup>12,13</sup>. A cascade develops as a sequence of elementary QED processes: photon emission by the electrons and positrons in the laser field alternates with pair production because of photon decay. A cloud or “cushion” of pair plasma in the laser pulse in front of the target has been observed in numerical simulations<sup>6</sup>. As the pair number becomes great, there is back reaction of the self-generated pair plasma on the laser-solid interaction. It has been demonstrated<sup>6,11</sup> that the produced pair plasma dramatically enhances laser field absorption and gamma-ray emission thereby reducing the HB front velocity. The pair motion in the combined laser and plasma fields with radiation reaction is rather complex that makes analytical treatment of pair plasma kinetics difficult. The analytical model for pair cushion in the nonlinear regime when the reflection of the laser pulse is strongly suppressed by the self-generated pair plasma has been recently proposed<sup>7</sup>.

<sup>a)</sup>Electronic mail: kost@appl.sci-nnov.ru

In our work we study the pair production in the regime when the number of the produced pairs is not sufficient to suppress laser reflection and to affect the laser-foil interaction. This is the case, for example, for interaction between extremely intense laser pulse and thin foils or for early stage of the laser interaction with thick solid target. The results of three dimensional particle-in-cell Monte Carlo (3D PIC-MC) simulations demonstrating the HB effect at interaction between a circularly polarized laser pulse and a foil are shown in Fig. 1. PIC-MC simulations including emission of hard photons and electron-positron pair production allow us to analyze the HB process at extremely high intensities. A similar numerical approach has been used in a number of works (see, e. g.<sup>6,19</sup>). To distill the physics of pair production and pair dynamics we consider extremely intense laser pulses. The simulation box is  $17.5\lambda \times 25\lambda \times 25\lambda$  corresponding to the grid size  $670 \times 125 \times 125$ ; the time step is  $0.005\lambda/c$ , where  $\lambda$  is the laser wavelength. In the simulation a quasi-rectangular ( $11.4\lambda \times 23\lambda \times 23\lambda$ ) circularly polarized laser pulse of intensity  $I_L = 2.75 \times 10^{24}$  W/cm<sup>2</sup> ( $a_0 = 1000$ ,  $\lambda = 1\mu\text{m}$ ) and  $I_L = 9.3 \times 10^{24}$  W/cm<sup>2</sup> ( $a_0 = 1840$ ,  $\lambda = 1\mu\text{m}$ ) interacts with a diamond foil ( $n_e = 6n_i = 1.1 \times 10^{24}\text{cm}^{-3}$ ,  $n_i/n_{cr} = 158$ ). The shape of the laser pulse is approximated as follows

$$E(x) \propto \frac{d}{dx} \left\{ \sin x \cos^2 \left[ \frac{\pi(x-x_s)^4}{2x_s^4} \right] \right\}, \quad (3)$$

where  $x_s = 5.7\lambda$  (the pulse duration is about 38 fs). The pulse has almost constant amplitude in the central area and promptly decreases at the distance  $x_s$  from the pulse center.

For  $a_0 = 1840$  parameters  $\mu = 1$  and the velocity of the HB front is a half of the speed of light. It is seen from Fig. 1 that the plasma is shifted towards the foil and the thin layer of electron-positron plasma is produced. The longitudinal phase space of the positrons produced at the laser-foil interaction is shown in Fig. 2 for two values of  $a_0$  ( $a_0 = 1000$  and  $a_0 = 1840$ ). In the high intensity regime ( $a_0 = 1840$ ) the positron distribution is strongly localized in the longitudinal phase space. In the low intensity regime ( $a_0 = 1000$ ) the positron distribution is sawtooth-like.

The electron-positron pair production can be roughly divided into three stages. At the initial stage the electron-positron pairs are produced from the photons emitted by the foil electrons. This stage can be described as follows. The laser pulse propagating in the positive direction of  $x$ -axis is reflected by the dense electron layer at the HB front. The layer electrons in a laser field emit a number of hard photons propagating in the same direction. The HB front outrun the photons emitted at the large angle to the  $x$ -axis so after that the photons move in vacuum region in the field of the incident and reflected laser radiation. In the HB front reference frame (“HB-frame”) these photons after escaping from plasma

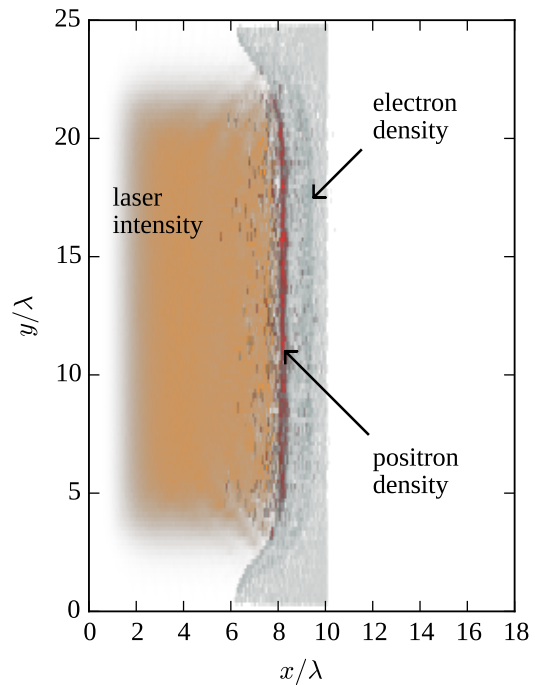


FIG. 1. The distribution of the laser intensity (orange color), the electron density (gray color) and the positron density (red color) in the  $x - y$  plane at  $z = 0$ ,  $t = 4\lambda/c$  for  $a_0 = 1840$ .

moves in the vacuum region in the negative direction of  $x$ -axis in the field of the circularly polarized standing wave. The structures, which are close to a counter-propagating wave or a standing wave, are efficient for pair creation<sup>12-14</sup> so that the photons decay and produce electron-positron pairs. In the second stage the number of pairs becomes so great that the number of high-energy photons emitted by the pairs exceeds the number of the external photons emitted by the foil electrons. In this case self-sustained QED cascade develops in the standing wave. In the final, third stage there is the back reaction of the self-generated electron-positron plasma on the laser-foil interaction. The electron-positron plasma becomes so dense that the significant part of the laser energy is absorbed by the pairs. In this paper we focus on the first two stages.

## II. FIELD STRUCTURE AND PAIR PRODUCTION IN THE VACUUM REGION

The incident laser field in the vacuum region can be approximated by the circularly polarized plane wave propagating along  $x$ -axis

$$\mathbf{E}_i = a_0 \frac{mc\omega_L}{e} (0, \cos \Phi, \sin \Phi), \quad (4)$$

$$\mathbf{B}_i = a_0 \frac{mc\omega_L}{e} (0, -\sin \Phi, \cos \Phi), \quad (5)$$

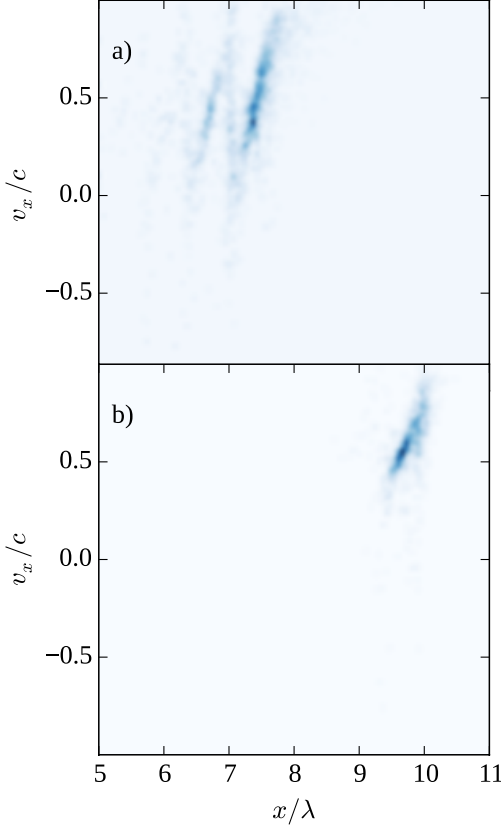


FIG. 2. The positron distribution in the plane  $x - v_x$ , for (a)  $a_0 = 1000$ ,  $t = 6.0\lambda/c$  and (b)  $a_0 = 1840$ ,  $t = 3.0\lambda/c$ .

where  $\Phi = \omega_L x/c - \omega_L t$ . The incident electromagnetic field in the HB-frame can be calculated with Lorentz transformation

$$\mathbf{E}'_i = a_0 (0, \cos(x' - t'), \sin(x' - t')), \quad (6)$$

$$\mathbf{B}'_i = a_0 (0, -\sin(x' - t'), \cos(x' - t')), \quad (7)$$

where prime symbol marks the quantities in the HB-frame. In this Section we use the dimensionless units, normalizing the time to  $1/\omega'$ , the length to  $c/\omega'$ , the momentum to  $mc$ , and the field amplitude to  $mc\omega'/e$ , where  $\omega' = \omega_L \gamma_{HB} (1 - v_{HB})$  is the frequency of the incident wave in the HB-frame and  $\gamma_{HB}^{-2} = 1 - v_{HB}^2$ . At the HB front position  $x' = 0$  the boundary condition is  $E'_y(x' = 0) = E'_z(x' = 0) = 0$ , where the perfect reflection in the HB-frame is assumed. The reflected laser radiation can be approximated as follows

$$\mathbf{E}'_r = a_0 (0, -\cos(x' + t'), \sin(x' + t')), \quad (8)$$

$$\mathbf{B}'_r = a_0 (0, \sin(x' + t'), \cos(x' + t')). \quad (9)$$

In the laboratory frame the reflected wave takes a form

$$\mathbf{E}_r = a_0 \omega_r (0, -\cos(\omega_r x + \omega_r t), \sin(\omega_r x + \omega_r t)), \quad (10)$$

$$\mathbf{B}_r = a_0 \omega_r (0, \sin(\omega_r x + \omega_r t), \cos(\omega_r x + \omega_r t)), \quad (11)$$

where

$$\omega_r = \omega_L \frac{1 - v_{HB}}{1 + v_{HB}}, \quad (12)$$

is the frequency of the reflected wave in the laboratory frame.

As the reflection coefficient is taken to be equal to 1 in the HB-frame, the standing wave is generated in the vacuum region:

$$\mathbf{E}' = 2a_0 (0, \sin x' \sin t', \sin x' \cos t'), \quad (13)$$

$$\mathbf{B}' = 2a_0 (0, \cos x' \sin t', \cos x' \cos t'). \quad (14)$$

The wavelength of the standing wave in the HB-frame is

$$\lambda' = 2\pi = \frac{\lambda}{\gamma_{hb} (1 - v_{hb})}. \quad (15)$$

The probability rate for photon emission by ultra-relativistic electrons and positrons in an electromagnetic field and the probability rate for electron-positron pair production via photon decay are given, respectively, by the formulas<sup>30</sup>

$$W_{rad} = \frac{\alpha a_S}{\varepsilon_e} \int_0^\infty dx \frac{5x^2 + 7x + 5}{3^{3/2} \pi (1+x)^3} K_{\frac{2}{3}} \left( \frac{2x}{3\chi_e} \right), \quad (16)$$

$$W_{rad} \approx \frac{5\alpha a_S}{2\sqrt{3}\pi\varepsilon_e} \chi_e, \quad \chi_e \ll 1, \quad (17)$$

$$W_{pair} = \frac{\alpha a_S 3^{-3/2}}{\pi \varepsilon_{ph}} \int_0^1 dx \frac{9 - x^2}{1 - x^2} K_{\frac{2}{3}} \left[ \frac{8\chi_{ph}^{-1}}{3(1-x^2)} \right] \quad (18)$$

$$W_{pair} \approx \frac{3^{3/2} \alpha a_S \chi_{ph}}{29/2 \varepsilon_{ph}} \exp\left(-\frac{8}{3\chi_{ph}}\right), \quad \chi_{ph} \ll 1, \quad (19)$$

where

$$\chi_{e,ph} = \frac{1}{a_S} \sqrt{(\varepsilon_{e,ph} \mathbf{E} + \mathbf{p}_{e,ph} \times \mathbf{B})^2 - (\mathbf{p}_{e,ph} \cdot \mathbf{E})^2} \quad (20)$$

is the key QED parameter determining the photon emission ( $\chi_e$ ) and the pair production ( $\chi_{ph}$ )<sup>31</sup>,  $a_S = eE_S/(mc\omega') = mc^2/\hbar\omega'$  is the normalized QED critical field,  $E_S = m^2 c^3/(\hbar e)$ ,  $\varepsilon_{e,ph}$  is the energy of the electron (positron) and photon, respectively,  $\mathbf{p}_{e,ph}$  is the momentum of the electron (positron) and photon, respectively,  $\hbar$  is the Planck constant.

The dependence of the pair production probability on  $\chi$  is sharp in the limit  $\chi \ll 1$ . Therefore we can suppose that the most of the pairs are produced near the points in the spacetime where  $\chi$  peaks. If the photon momentum is  $\mathbf{p}' = \varepsilon_{ph} (\cos \alpha, \sin \alpha \cos \beta, \sin \alpha \sin \beta)$  then  $\chi$  for the circularly polarized standing wave given by Eqs. (13), (14) takes a form in the HB-frame after some trigonometrical transformations

$$\chi_{ph} = \frac{\varepsilon_{ph} a_0}{a_S} \sqrt{1 - \sin^2 \phi \sin^2 \alpha}, \quad (21)$$

where  $\phi = \beta - t'$ . It follows from Eq. (21) that  $\chi$  peaks at  $\phi = \pm\pi n$  or  $\alpha = \pm\pi l$ ,  $n, l = 0, 1, 2, \dots$  and it does not depend on  $x'$ . For given value of  $\beta$  there is always the value of  $t'$  at which  $\phi = \pm\pi n$ . If the photon emission is axially symmetrical ( $\beta$  is uniformly distributed from 0 to  $2\pi$ ) then we can suppose that the pair number decreases with increasing the distance from the HB front towards the vacuum region as a result of photon flux attenuation.

### III. PARTICLE MOTION IN A STANDING CIRCULARLY POLARIZED WAVE

In this Section we study the motion of the electrons and positrons in the vacuum field in the HB-frame. The field can be approximated by the circularly polarized standing wave defined by Eqs. (13) and (14). Our treatment is based on the classical approach in order to obtain analytical solutions. In the QED approach the particle momentum suddenly changes because of recoil effect caused by photon emission. However even in the limit  $\chi \gg 1$  the particle energy much greater than the mean change in its energy because emission of one photon:  $\langle \varepsilon_{ph} \rangle < I_{rad}(\chi \rightarrow \infty) / W_{rad}(\chi \rightarrow \infty) \approx 0.25 \ll \varepsilon_e$ , where  $I_{rad}$  is the total intensity of the photon emission. It is demonstrated by numerical simulations<sup>18,22</sup> that the spatial distributions of the electrons calculated in the classical approach and in QED approach are similar even for extremely strong electromagnetic fields.

In the classical approach the positron motion is governed by equations

$$\frac{d\mathbf{p}}{dt} = \mathbf{F}_L - \mathbf{v}F_R, \quad (22)$$

$$\frac{d\mathbf{r}}{dt} = \frac{\mathbf{p}}{\gamma}, \quad (23)$$

$$\mathbf{F}_L = \mathbf{E} + \mathbf{v} \times \mathbf{B}, \quad (24)$$

$$F_R = \mu a_S^2 \chi_e^2 G(\chi_e), \quad (25)$$

$$\chi_e^2 = a_S^{-2} \gamma^2 \left[ (\mathbf{E} + \mathbf{v} \times \mathbf{B})^2 - (\mathbf{v} \cdot \mathbf{E})^2 \right],$$

where  $F_R/G(\chi_e)$  is the leading term of the radiation reaction force in the classical limit<sup>32</sup>,  $\mu = 2\omega'e^2/(3mc^3)$ ,  $G(\chi_e) = I_{rad}(\chi_e)/I_{rad}(\chi_e = 0)$  is the QED factor introduced in order to take into account the decreasing of the radiation power and the radiation reaction force in the quantum limit with increasing of  $\chi_e$ <sup>12,15,38</sup>. For the sake of convenience, hereinafter, the prime symbol are omitted for the quantities in the HB-frame.

It is shown for a rotating electric field<sup>34,35</sup> that there is a stationary trajectory attracting the other trajectories. The field has to be strong enough so that the electrons and positrons move in the radiation reaction regime. Regardless of the initial momentum a positron quickly reaches stationary trajectory which is the rotation with the field frequency. The phase shift between the field and the positron velocity is set so that the work

done by the electric field is completely compensated by the radiative losses.

We extend the Zeldovich model<sup>34</sup> to the configuration of the rotating homogeneous electric and magnetic fields, which are parallel to each other:

$$\mathbf{E} = E_0(0, \sin t, \cos t), \quad \mathbf{B} = B_0(0, \sin t, \cos t). \quad (26)$$

The electric and magnetic fields rotate in the plane  $y - z$  with the unit frequency  $\omega' = 1$ . Like in the Zeldovich model we assume that the positron rotates in the plane  $y - z$  with the constant velocity  $v_\perp$  and frequency  $\omega' = 1$  but it additionally moves along  $x$ -axis with the constant velocity  $v_x$ . Balancing the forces along  $x$ -axis and in the  $y - z$  plane (along the centrifugal force and along the transversal velocity, respectively) we get

$$\frac{dp_x}{dt} = v_\perp B_0 \sin \varphi - v_x F_R = 0, \quad (27)$$

$$\frac{dp_y}{dt} = E_0 \sin \varphi + B_0 v_x \cos \varphi = \gamma v_\perp, \quad (28)$$

$$\frac{dp_z}{dt} = E_0 \cos \varphi - v_x B_0 \sin \varphi - v_\perp F_R = 0, \quad (29)$$

$$F_R = \mu G(\chi_e) W^2 \gamma^2 (1 - v_\perp^2 \cos^2 \varphi), \quad (30)$$

$$\chi_e = a_S^{-1} W \gamma \sqrt{1 - v_\perp^2 \cos^2 \varphi}, \quad (31)$$

$$\frac{d\mathbf{r}}{dt} = \frac{\mathbf{p}}{\gamma}, \quad (32)$$

where it is assumed that  $z$ -axis is directed along the transverse component of the positron velocity,  $\mathbf{v}_\perp$ , so that the centrifugal force is directed along the  $y$ -axis,  $\varphi$  is the angle between  $\mathbf{v}_\perp$  and  $\mathbf{E}$ ,  $\gamma^{-2} = 1 - v_x^2 - v_\perp^2$  is the reverse squared relativistic Lorentz factor of the positron,  $W^2 = E_0^2 + B_0^2$ . The first equation represents the balance between the Lorentz force and the radiation reaction force along  $x$ -axis, the second one represents the balance between the centrifugal force and the Lorentz force. For ultra-relativistic motion  $\gamma \gg 1$  ( $v_x \approx 1 - v_\perp^2$ ) Eqs. (27)-(30) can be reduced to the system of equations for  $\gamma$ ,  $v_\perp$  and  $\cos \varphi$ :

$$v_\perp B_0 = \sqrt{\frac{1 - v_\perp^2}{1 - \cos^2 \varphi}} F_R(\gamma, v_\perp, \cos \varphi), \quad (33)$$

$$\gamma v_\perp = E_0 \sqrt{1 - \cos^2 \varphi} + B_0 \sqrt{1 - v_\perp^2} \cos \varphi, \quad (34)$$

$$v_\perp E_0 \cos \varphi = F_R(\gamma, v_\perp, \cos \varphi), \quad (35)$$

where  $F_R$  is given by Eq. (30). The third equation can be derived by summation of Eq. (27) multiplied by  $v_x$  and Eq. (29) multiplied by  $v_\perp$ . It demonstrates that the radiative losses are completely compensated by the work done by the electric field, hence  $F_R \leq E_0$ . Note that the useful relations  $\gamma v_\perp E_0 = W^2 \sin \varphi$  and  $v_x = (B_0/E_0) \tan \varphi$  can be derived from Eqs. (33)-(35).

In the limit of high field the radiation reaction is strong and  $F_R \approx E_0$ ,  $\varphi \ll 1$ ,  $v_x \ll 1$  and the solution of Eqs. (33)-(35) can be written as follows

$$\varphi \approx \frac{E_0 \gamma}{W^2} \ll 1, \quad (36)$$

$$v_x \approx \frac{B_0}{E_0} \varphi \ll 1, \quad (37)$$

$$\chi_e \approx \frac{\gamma^2}{a_S}, \quad (38)$$

$$\gamma = \varepsilon_e \approx \left[ \frac{E_0}{\mu G(\chi_e)} \right]^{1/4}, \quad (39)$$

where it is assumed that  $B_0 \lesssim E_0$ . It follows from Eqs. (36) and (39) that the radiation reaction regime corresponds to the condition  $\epsilon_R \equiv E_0^3 G \mu \gg 1$ . In order to explicitly write expressions for  $\varphi$ ,  $v_x$  and  $\gamma$  we have to solve Eq. (38) for  $\chi_e$

$$\chi_e^2 G(\chi_e) = \frac{E_0}{\mu a_S^2}. \quad (40)$$

Eqs. (36) and (39) are reduced to the formulas derived by Zeldovich<sup>34</sup> in the limit  $B_0 = 0$  and  $G = 1$ .

More accurate value of  $\gamma$  (for arbitrary value of  $\varphi$  and  $\epsilon_R$  i.e. not only for the radiation reaction regime) can be found in the limit  $B_0 \ll E_0 \epsilon_R$  ( $v_x \ll 1$ ) from equation

$$E_0^2 - \gamma^2 \frac{E_0^2}{W^2} \approx \mu^2 G^2(\chi_e) \gamma^8, \quad (41)$$

$$\chi_e \approx \frac{\gamma^2}{a_S}. \quad (42)$$

It should be noted that Eq. (41) for  $\gamma$  is similar to one for the electron energy in the rotating electric field<sup>34</sup> and in the running circularly polarized wave<sup>8,9</sup> for  $G(\chi_e) = 1$ . In the limit for the radiation reaction regime ( $\epsilon_R \gg 1$ ) Eq. (41) is reduced to Eq. (39). In the opposite limit, when the radiation reaction can be neglected,  $\gamma \approx W$  and  $\gamma \approx E_0$  for  $B_0 = 0$  in agreement with the known results<sup>34</sup>.

Combining Eqs. (38) and (41) the equation for  $\chi_e$  can be derived

$$\frac{G^2(\chi_e) \chi_e^4}{W^2 a_S^{-1} - \chi_e} \approx \frac{E_0^2}{\mu^2 W^2 a_S^3}, \quad (43)$$

In the limit  $W^2 a_S^{-1} \gg \chi_e$  ( $\epsilon_R \gg 1$ ) Eq. (43) is reduced to Eq. (40).

The description with the averaged radiation reaction force with QED factor  $G(\chi_e)$  can be used when the number of the photons emitted during interaction and during the characteristic time of the field ( $1/\omega'$ ) is large:  $W_{rad} \gg 1$ , where  $\tau_{rad} \sim W_{rad}^{-1}$  is the characteristic time of the photon emission. The model is not valid when the electric field is too weak and Eq. (35) is not fulfilled. In other words, the radiative losses has to be compensated by the work done by the electric field. It follows from the obtained result that the stationary trajectory in the rotating electric and magnetic field is helical so that the positron drifts along  $x$ -axis with the constant velocity

$v_x$  and rotates in  $y-z$  plane with phase shift between the field and the transverse component of the velocity,  $\varphi$ . The stationary trajectory ( $\mathbf{r}^z, \mathbf{p}^z$ ) in the the radiation reaction regime ( $\epsilon_R \gg 1$ ) can be approximated as follows

$$x^z \approx v_x t, \quad (44)$$

$$y^z \approx \cos(t + \varphi), \quad (45)$$

$$z^z \approx -\sin(t + \varphi), \quad (46)$$

$$p_x^z = v_x \gamma^z \approx \frac{B_0}{W^2} \gamma^z, \quad (47)$$

$$p_y^z \approx \gamma^z \sin(t + \varphi), \quad (48)$$

$$p_z^z \approx \gamma^z \cos(t + \varphi), \quad (49)$$

$$\gamma^z \approx \left[ \frac{E_0}{\mu G(\chi_e)} \right]^{1/4}, \quad (50)$$

where  $\varphi$  and  $v_x$  are given by Eqs. (36) and (37), respectively.

The positron trajectory given by Eqs. (36)-(39) is calculated for homogeneous electric and magnetic fields. However the solution can be also used to describe the positron motion in the standing circularly polarized wave far from the electric node (the antinode of  $\mathbf{B}$ ). This is because of the slow motion of the positron along  $x$ -axis ( $v_x \ll 1$ ) so that the positron has enough time to switch to the stationary trajectory given by Eqs. (44)-(49) and determined by the local values of the fields. The trajectory of the positron created near the magnetic node of the standing wave can be calculated by taking into account the dependence of  $E_0$  and  $B_0$  on  $x$  in Eqs. (27)-(32), where  $E_0 = 2a_0 \sin x$ ,  $B_0 = 2a_0 \cos x$  and  $W = 2a_0$ . The longitudinal coordinate can be found from the equation of motion:  $dx/dt = v_x$  :

$$\int_0^{x^z} \frac{d\xi}{v_x(E_0(\xi), B_0(\xi))} = t, \quad (51)$$

where  $v_x$  is the solution of Eqs. (33)-(35).  $v_x$  can be approximated by using of Eq. (37) as follows:

$$v_x \approx u \cos x |\sin x|^{1/4} \text{sign}(\sin x), \quad (52)$$

where  $u = (8a_0^3 \mu G(\chi_e))^{-1/4}$ ,  $\chi_e$  is the solution of Eq. (43) for  $E_0 \approx 2a_0$ ,  $\text{sign}(x) = -1$  for  $x < 0$ ,  $\text{sign}(x) = 0$  for  $x = 0$  and  $\text{sign}(x) = 1$  for  $x > 0$ . The dependence of  $v_x$  on  $x$  is shown in Fig. 3. Therefore, the positron trajectory near the magnetic node of the standing wave takes a form  $\mathbf{r} \approx \mathbf{r}_0 + \mathbf{r}^z(t, E_0(x(t)), B_0(x(t)), \varphi(x(t)))$ ,  $\mathbf{p} \approx \mathbf{p}^z(t, E_0(x(t)), B_0(x(t)), \varphi(x(t)))$ , where the constant  $\mathbf{r}_0$  is determined by the initial conditions. Note that such constant is absent in the expression for  $\mathbf{p}$  since all positrons locating at the same position on the stationary trajectory have the same momentum. Evidently, for the electrons  $v_x$  is the same as that for the positrons while  $\mathbf{v}_\perp$  is opposite to that of the positrons.

The equations of motion are solved numerically with the radiation reaction force for the positron being initially near the magnetic node ( $x(t=0) = 0.497\pi$ ,

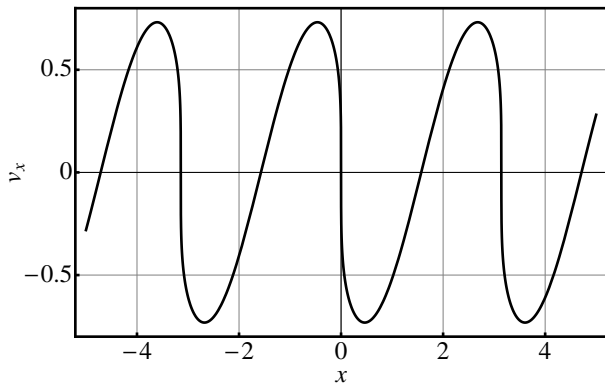


FIG. 3.  $v_x(x)$  calculated from Eq. (52) for  $u = 1$ .

$p(t = 0) = 0$ ) of the standing wave with  $a_0 = 1000$ . First we solve Eqs. (22)-(25) neglecting the suppression of the radiation reaction force ( $G = 1$ ). The values of  $\gamma(t)$ ,  $v_x(t)$  and  $\chi_e(t)$  obtained from numerical solution of equations of motion and ones estimated from Eqs. (36)-(39) are shown in Fig. 4, where in the estimations  $E_0 = 2a_0 \sin x(t)$ ,  $B_0 = 2a_0 \cos x(t)$  and  $x(t)$  is retrieved from the numerical solution. It is seen from Fig. 4(a) that the model prediction is in a very good agreement with the numerical solution of the equations of motion. The better agreement is achieved (see Fig. 4(b)) when Eq. (41) is used instead of Eq. (39). It is interesting to note that even near the electric node ( $x \approx 0$ ) the agreement is still fairly good.

We also solve the equations of motion numerically for the positron with the same initial condition taking into account QED suppression of the radiation reaction force, where the approximation  $G(\chi_e) \approx (1 + 18\chi_e + 69\chi_e^2 + 73\chi_e^3 + 5.804\chi_e^4)^{-1/3}$  proposed in Ref.<sup>38</sup> is used. The values of  $\gamma(t)$ ,  $v_x(t)$  and  $\chi_e(t)$  obtained from numerical solution of equations of motion and ones estimated from Eqs. (36)-(38), (40) are shown in Fig. 5(a) and ones estimated from Eqs. (36)-(38), (43) are shown in Fig. 5(b). In the estimations  $E_0 = 2a_0 \sin x(t)$ ,  $B_0 = 2a_0 \cos x(t)$ , where  $x(t)$  is retrieved from the numerical solution of the equations of motion. It is seen from Fig. 5(a) that the agreement between the quantities calculated numerically and the estimated ones is not so good as in the case  $G = 1$ . The discrepancy is caused by strong radiation reaction suppression ( $G \ll 1$ ). It is seen from Fig. 6 that the radiation reaction parameter  $\epsilon_R(t) = \mu G(\chi_e(t)) E_0^3(t)$  determining the transition to the radiation reaction regime decreases in about 20 times when the suppression is taken into account. In this case the parameter is close to 5 and is not sufficient to ensure the required accuracy of the approximation corresponding to the radiation reaction regime and described by Eqs. (36)-(38), (40). Significant improvement of the accuracy can be achieved when more general Eq. (43) is used instead of Eq. (40) (see Fig. 5(b)).

It follows from Fig. 5 that  $\gamma \sim 1200$  and  $\chi_e \sim 4$  in

the case when the radiation reaction suppression is included. The positron energy and the parameter  $\chi_e$  are higher in several times than ones in the case  $G = 1$  (see Fig. 4). The probability rate for photon emission given by Eq. (16) is  $W_{rad} \sim 8$  for  $\gamma \sim 1200$  and  $\chi_e \sim 4$ . Therefore the positron passing from the magnetic node to the electric one during  $t_{int} \sim 11$  emits about  $N_{ph} \sim t_{int}/\tau_{rad} \sim t_{int}W_{rad} \sim 90 \gg 1$  photons and the approximation with the averaged radiation reaction force by means of factor  $G$  can be applied.

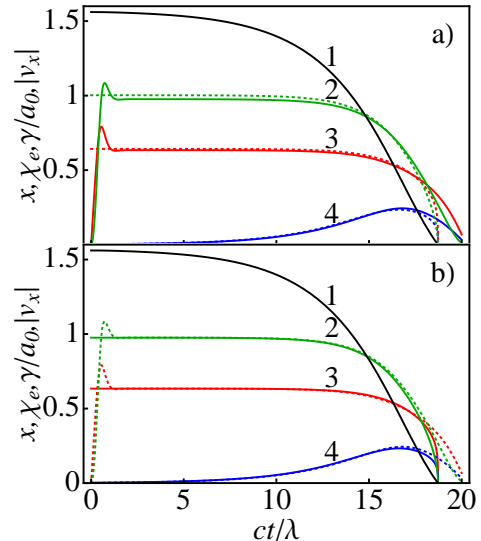


FIG. 4. The approximation  $G = 1$  (the QED suppression of the radiation reaction is neglected).  $x(t)$  (solid black line 1),  $\chi(t)$  (solid green line 2),  $\gamma(t)/a_0$  (solid red line 3),  $v_x(t)$  (solid blue line 4) calculated numerically by solving Eqs. (22)-(25) for the positron with the initial condition  $x(t = 0) = 0.497\pi$ ,  $p(t = 0) = 0$  in the standing wave (Eqs. (13) and (14)) with  $a_0 = 1000$ .  $\chi(x(t))$  (dashed green line 2),  $\gamma(x(t))/a_0$  (dashed red line 3),  $v_x(x(t))$  (dashed blue line 4) are calculated from (a) Eqs. (36)-(39) and (b) from Eqs. (36)-(38), (41), where  $E_0 = 2a_0 \sin x(t)$ ,  $B_0 = 2a_0 \cos x(t)$ .  $x(t)$  is retrieved from the numerical solution and shown by the solid black line 1.

It follows from Eqs. (52) that the longitudinal velocity of the positrons and electrons created with small momentum in the standing circularly polarized wave is directed from the magnetic nodes ( $x = \pm\pi(n + 1/2)$ ,  $n = 0, 1, 2, \dots$ , where  $\mathbf{B} = 0$  and the electric field amplitude peaks) to the electric ones ( $x = \pm\pi n$ ,  $n = 0, 1, 2, \dots$ , where  $\mathbf{E} = 0$  and the magnetic field amplitude peaks). Hence, the magnetic nodes are unstable for the positrons and electrons while the electric nodes are stable for them (see Fig. 3). In the magnetic nodes the positrons and electrons perform circular motion in the rotating electric field. In the electric nodes the positrons and electrons move in the rotating magnetic field. This motion is complex and can be qualitatively presented as the superposition of the fast cyclotron rotation (rotation axis is perpendicular to the  $x$ -axis) and slow drift. The fre-

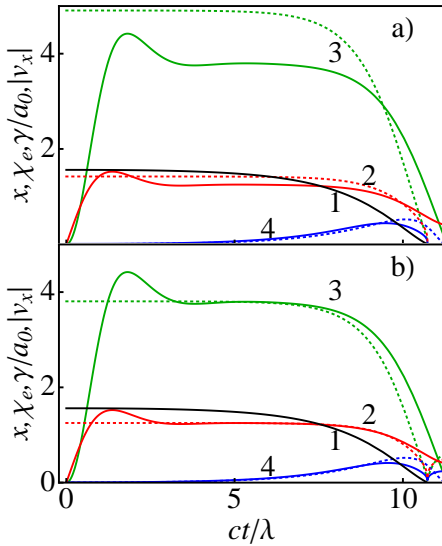


FIG. 5. The case when the QED suppression of the radiation reaction is taken into account.  $x(t)$  (solid black line 1),  $\gamma(t)/a_0$  (solid red line 2),  $\chi(t)$  (solid green line 3),  $v_x(t)$  (solid blue line 4) calculated numerically by solving Eqs. (22)-(25) for the positron with the initial condition  $x(t=0) = 0.497\pi$ ,  $p(t=0) = 0$  in the standing wave (Eqs. (13) and (14)) with  $a_0 = 1000$ .  $\chi(x(t))$  (dashed green line 3),  $\gamma(x(t))/a_0$  (dashed red line 2),  $v_x(x(t))$  (dashed blue line 4) are calculated from (a) Eqs. (36)-(39), (40) and (b) from Eqs. (36)-(38), (43), where  $E_0 = 2a_0 \sin x(t)$ ,  $B_0 = 2a_0 \cos x(t)$ .  $x(t)$  is retrieved from the numerical solution and shown by the solid black line 1.

quency of the cyclotron rotation in the magnetic field is much higher than the field frequency  $\omega_B \approx 2a_0\omega'/\gamma \gg \omega'$  since the positrons and electrons move in the radiation reaction regime for  $a_0 > 300$  so that  $\gamma/a_0 \sim \epsilon_R^{-1/4} \ll 1$  (see Eq. (39) and Refs.<sup>8,9,34</sup>).

When the number of the electron-positron pairs becomes large they produce more photons than ones arrived from the electron layer. As a result the self-sustained QED cascade characterized by exponential growth of the pair number in time can develop. It is demonstrated<sup>16</sup> that the cascade growth rate is maximal in the magnetic nodes of the circularly polarized standing wave. However it is discussed above that the the pair positions is unstable in the magnetic nodes and is stable in the electric ones. The pair density profile is determined by the trade off between the pair production effect and the pair drift. Therefore the density of the electron-positron plasma may peak at the electric and magnetic nodes as the pairs production is the most efficient at the magnetic nodes while the pairs after creation are attracted to the electric nodes.

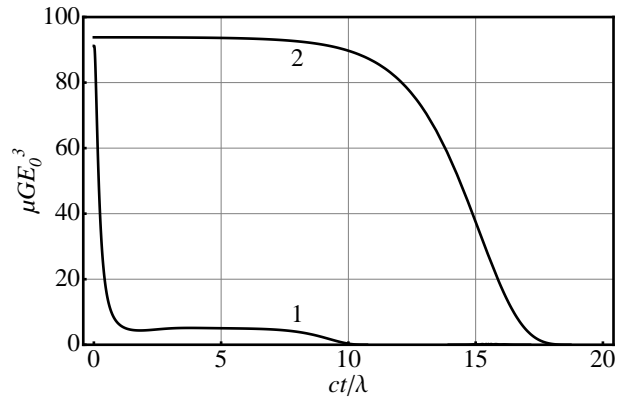


FIG. 6. The radiation reaction parameter  $\epsilon_R(t) = \mu G(\chi_e(t)) E_0^3(t)$  for the positron with the initial condition  $x(t=0) = 0.497\pi$ ,  $p(t=0) = 0$  in the standing wave (Eqs. (13) and (14)) with  $a_0 = 1000$  in the case when the QED suppression of the radiation reaction is taken into account (line 1) and in the approximation  $G = 1$  when the suppression is neglected (line 2).

#### IV. NUMERICAL SIMULATIONS

The field of the incident wave can be retrieved from  $E_y + B_z$  and the field of the reflected wave can be retrieved from  $E_y - B_z$  calculated in the numerical simulations. To compare the analytical results with the numerical ones it is convenient to use other dimensionless units, normalizing the time to  $1/\omega_L$ , the length to  $c/\omega_L$ , and the field amplitude to  $m c \omega_L / e$ . It follows from Eqs. (4), (5), (10), (11) that

$$E_{i,y} + E_{r,y} + B_{i,z} + B_{r,z} = 2a_0 \cos(x-t), \quad (53)$$

$$E_{i,y} + E_{r,y} - B_{i,z} - B_{r,z} = 2a_0 \omega_r \times \cos[\omega_r(x+t)]. \quad (54)$$

The HB front velocity and the frequency of the reflected wave can be estimated by using Eqs. (1), (2) and (12). Then for the simulation parameters we get:  $\mu = 1.84$ ,  $v_{HB} \approx 0.35$ , and  $\omega_r \approx 0.48$  for  $a_0 = 1000$ , while  $\mu = 1$ ,  $v_{HB} = 1/2$  and  $\omega_r \approx 0.33$  for  $a_0 = 1840$  that is close to the simulation results, namely from the periods of the wave  $E_y - B_z$  (see Figs. 7 and 8) we obtain  $\omega_r \approx 0.5$  for  $a_0 = 1000$  and  $\omega_r \approx 0.4$  for  $a_0 = 1840$ . According to the model assumptions the reflection in the HB-frame is perfect so that the reflection coefficient in the laboratory frame is equal to  $r = \max[(E_y - B_z)/(E_y + B_z)] = \omega_r$ . This is also in a good agreement with the results of the numerical simulations (see Figs. 7 and 8). Therefore the approximation of the structure of the electromagnetic field in the vacuum region (in front of the foil) as a standing wave can be used for estimations.

The positron number as a function of time is shown in Fig. 9. It follows from Fig. 9 that the exponential growth representing QED cascading starts almost from the beginning. The cascade develops in the circularly polarized standing wave generated in the HB-frame in front

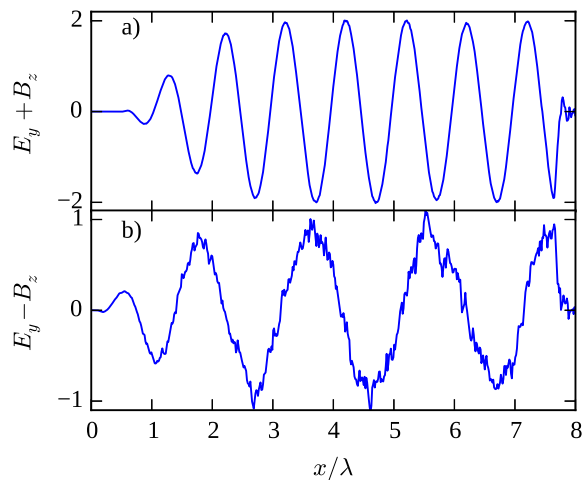


FIG. 7. (a)  $E_y + B_z$  and (b)  $E_y - B_z$  as a function of  $x$  in front of the foil for  $a_0 = 1000$  at  $t = 6\lambda/c$ .

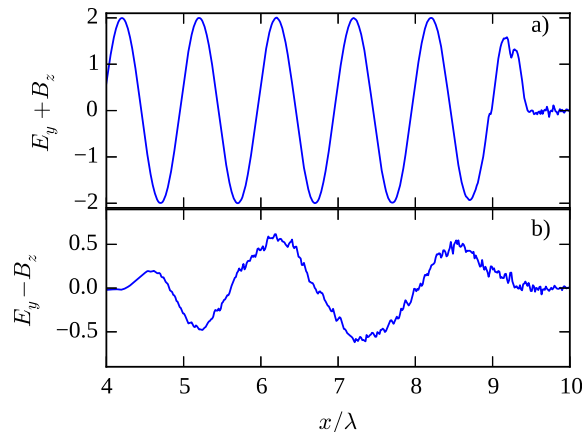


FIG. 8. (a)  $E_y + B_z$  and (b)  $E_y - B_z$  as a function of  $x$  in front of the foil for  $a_0 = 1840$  at  $t = 4\lambda/c$ .

of the foil. The cascade growth rate can be estimated from the figure:  $\Gamma \approx 0.6$  for  $a_0 = 1000$  and  $\Gamma \approx 1.3$  for  $a_0 = 1840$ , where the cascade growth rate is normalized to the frequency of the standing wave in the HB-frame,  $\omega' = \omega_L \gamma_{HB} (1 - v_{HB})$ . The obtained values of  $\Gamma$  are slightly less than that calculated in Ref.<sup>37</sup> by numerical simulation for the rotating electric field and for the circularly polarized standing wave ( $\Gamma \approx 0.8$  for  $a_0 = 1000$  and  $\Gamma \approx 1.8$  for  $a_0 = 1840$ , see Fig. 2a in Ref.<sup>37</sup>). The reason is that the standing wave is not perfect in our case because the laser radiation reflection from the foil is not also perfect.

According to Eq. (13) the square of the electric field in the vacuum region in the HB-frame as a function of the

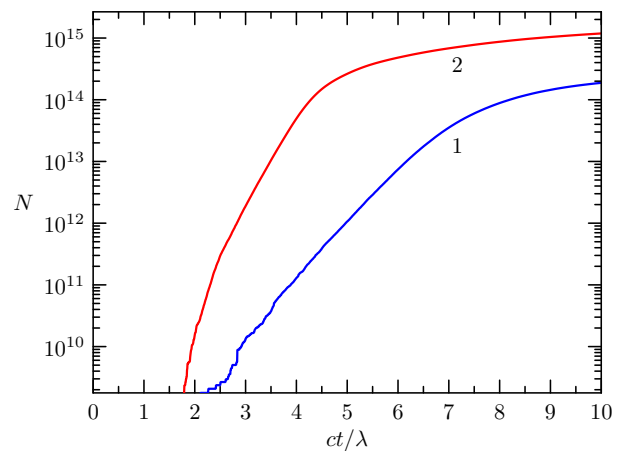


FIG. 9. Positron number as a function of time for  $a_0 = 1000$  (line 1) and  $a_0 = 1840$  (line 2).

space-time position in the laboratory frame takes a form:

$$\begin{aligned} (\mathbf{E}')^2 &= (2a_0\omega')^2 \sin^2(\omega'x') \\ &= (2a_0)^2 \frac{1 - v_{HB}}{1 + v_{HB}} \sin^2\left(\frac{x - v_{HB}t}{1 + v_{HB}}\right). \end{aligned} \quad (55)$$

To calculate the fields in the HB-frame we can apply Lorentz transformation to the field distribution retrieved from the numerical simulations with  $v_{HB} \approx 0.35$  for  $a_0 = 1000$  and  $v_{HB} = 0.5$  for  $a_0 = 1840$ . Thus the positions of nodes and antinodes in the laboratory reference frame can be easily found from the distribution of  $(\mathbf{E}')^2$ . The squared electric and magnetic fields in the HB-frame,  $(\mathbf{E}')^2$  and  $(\mathbf{B}')^2$ , as a function of  $x$ , the positron distribution in the plane  $x - v_x$  and the positron density at the axis  $y = z = 0$  as a function of  $x$  are shown in Fig. 10 for  $a_0 = 1000$  and  $t = 6.4\lambda/c$  and in Fig. 11 for  $a_0 = 1840$  and  $t = 4.0\lambda/c$ . It is seen from Fig. 11 that for strong laser field with  $a_0 = 1840$  the most of the positrons are created in front of the foil near the first magnetic node of the standing wave because the most of the photons, which are emitted from the foil and initiating the cascade, decay already in the first period of the standing wave. In this case the pair production effects dominate over the pair drift so that the number of the pairs produced at the magnetic nodes is higher than that drift to the electric nodes<sup>16</sup>. In other words, the time of the particle doubling is less than the time which takes for the particles to pass from a magnetic node to the neighboring electric nodes. For  $a_0 = 1000$  the probability of the pair production is lower than for  $a_0 = 1840$  and the positrons are located in the several wavelengths in front of the foil near the electric and magnetic nodes (see Fig. 10 (c)) that is in the qualitative agreement with the predictions formulated in the previous Section. Small shift of the maximums of the density profile from the exact position of the nodes can be caused by fact that the reflection is not perfect so that the wave in the HB-frame is not exactly standing.



It follows from Figs. 10 and 11 that the longitudinal velocity of the positrons is close to the HB front velocity at the magnetic nodes and the velocity distributed within wide range near the electric node. For  $a_0 = 1000$  the positron distribution is sawtooth-like in  $x - v_x$  plane (see Fig. 10(b)). Therefore, in the HB front frame, the longitudinal positron velocity increases towards the HB front from one electric node to another electric node reaching  $v_x = 0$  at the magnetic nodes. This is in qualitative agreement with Eq. (52) describing sawtooth-like distribution (see Fig. 3). The longitudinal dynamics of the secondary electrons is the same as that of the positrons.

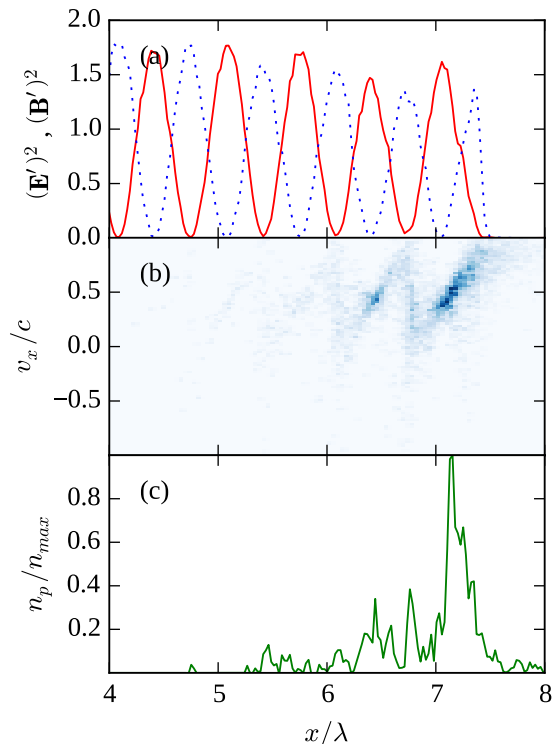


FIG. 10. (a) The squared electric and magnetic fields in the HB-frame,  $(\mathbf{E}')^2$  (solid red line) and  $(\mathbf{B}')^2$  (dashed blue line), as a function of  $x$ , (b) the positron distribution in the plane  $x - v_x$  and (c) the positron density along the  $x$ -axis as a function of  $x$  for  $a_0 = 1000$  and  $t = 6.4\lambda/c$ .

## V. DISCUSSIONS AND CONCLUSIONS

It is demonstrated that numerous electron-positron pairs are produced in the hole-boring regime of interaction between a foil and laser pulse with intensities higher than  $10^{24} \text{W cm}^{-2}$ . The pair production scenario can be roughly divided into three stages: (i) cascade initiation by the photons emitted from the foil electrons; (ii) self-sustained QED cascading in the standing wave; (iii) the back reaction of the produced pair plasma on the laser-foil interaction. In the first two stages the pairs

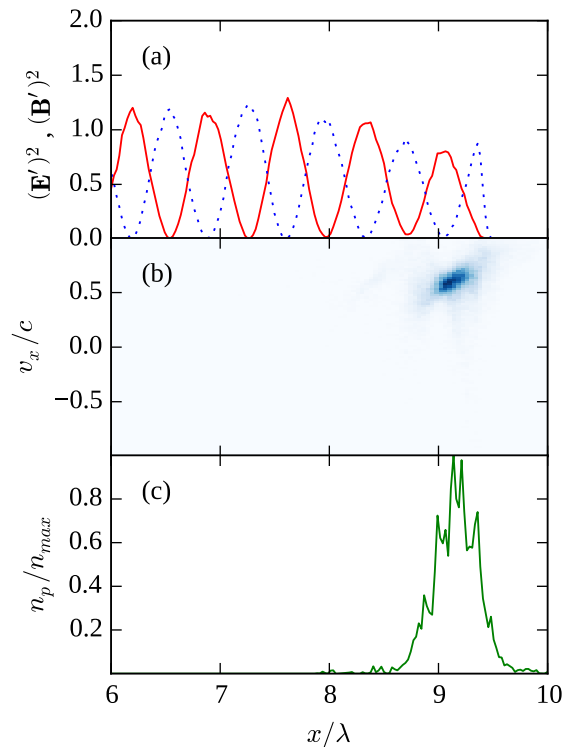


FIG. 11. (a) The squared electric and magnetic fields in the HB-frame,  $(\mathbf{E}')^2$  (solid red line) and  $(\mathbf{B}')^2$  (dashed blue line), as a function of  $x$ , (b) the positron distribution in the plane  $x - v_x$  and (c) the positron density along the  $x$ -axis as a function of  $x$  for  $a_0 = 1840$  and  $t = 4.0\lambda/c$ .

are mainly located in the vacuum region in front of the foil where the incident and reflected laser waves interfere. When the number of the produced electron-positron pairs is not very large the field structure in the vacuum region is close to the standing circularly polarized wave in the hole-boring front reference frame. The electron-positron plasma is mainly produced as a result of QED cascading in the standing wave.

The analytical model for the dynamics of the electrons and positrons in the rotating electric field with radiation reaction is extended to the rotating electric and magnetic fields which are parallel to each other. The model proposed by Zeldovich<sup>34</sup> predicts the stationary trajectory attracting the electron trajectories in the rotating electric field when the radiation reaction is strong. On such trajectory the work done by the electric field is balanced by the radiative losses. The particle performs circular motion and the energy balance is controlled by the phase shift between the electric field and the particle velocity. In the case of the rotating electric and magnetic fields, which are parallel to each other, the stationary trajectory also exists and is helical-like with infinite motion along the axis perpendicular to the plane of the field rotation. The dynamics in the circularly polarized standing wave is more complex<sup>20,38</sup>. Moreover, the particle

motion can be stochastic and the attractor accumulating the trajectories in the phase space is located only at the electric node. The attractors are recently studied in the field of standing waves of various configurations<sup>20,22,24,38</sup>. Our model allows one to calculate the particle trajectory near the magnetic node of the standing wave. It is shown that the trajectory of the electron and positrons near the magnetic node is close to the stationary trajectory in the local electric and magnetic fields. The model includes the QED effect of the radiation reaction suppression because of the reduction of the total power radiated by the particle in the quantum regime<sup>12,15,38</sup>.

The calculated trajectories are used to analyze the positron density distribution in the standing wave. It follows from the model that the positron density peaks at the nodes and antinodes of the standing wave because the electron-positron pairs are mainly produced at the magnetic nodes as the cascade growth rate peaks there and the produced pairs drift to the electric nodes as the magnetic nodes are unstable for them. The positron distribution in  $x$ - $v_x$  plane is sawtooth-like and the longitudinal velocity of the positrons is equal to HB-front velocity at the magnetic nodes. Near the electric nodes the motion of the electrons and positrons is close to the superposition of the drift and the rotation so that the longitudinal velocity varies within the wide range. This is in agreement with the results of the numerical simulations.

In the case of high laser intensity ( $a_0 = 1840$ ) the density peaks at the magnetic node closest to the HB front. The reason is that the high-energy photons emitted by the foil electrons decay rapidly and cannot initiate cascade far from the HB-front. The number of the pairs in the electric nodes is much smaller than that in the magnetic ones because near the magnetic node the pair production rate dominates over the pair loss rate due to the drift.

The first stage representing the cascade initiation is not pronounced in Fig. 9. One of the reason is that the number of the high-energy photons emitted by the electron layer is not very large because the laser field is strongly suppressed in the layer and the layer electrons are not accelerated so efficiently as the positrons and the secondary electrons in the vacuum region in front of the foil. Therefore the number of the high-energy photons emitted by the pairs and participating in cascading will exceed the number of the photons emitted by the foil electrons in very short period of time so that the duration of the first stage may be small.

When the pair number becomes great the produced electron-positron plasma can absorb the laser radiation and affect the dynamics of the laser-foil interaction. The manifestation of such nonlinear stage (the third stage) can be seen in Figs. 10(a) and 11(a) where the standing wave is slightly attenuated towards the HB front. The transition between the second and the third stage can be seen in Fig. 9 as a saturation of the pair number growth. The transition occurs at  $t \approx 7.5\lambda/c$  for  $a_0 = 1000$  and for  $t \approx 4.5\lambda/c$  for  $a_0 = 1840$ . The analytical model of the

third stage has been proposed in Ref.<sup>7</sup>. It is based on one-dimensional solutions of the two-fluid (electron-positron) and Maxwell equations, including a classical radiation reaction term. The model predicts the vacuum gap with the standing wave structure between the pair ‘‘cushion’’ and the targets. However the model verification by self-consistent numerical simulations is still absent and the detailed analysis of the third stage with back reaction is needed.

## ACKNOWLEDGMENTS

This work was supported by the Russian Science Foundation Grant No. 16-12-10383.

- <sup>1</sup>V. Yanovsky *et al.* Opt Express **16**, 2109 (2008).
- <sup>2</sup>G. Mourou, T. Tajima, S. V. Bulanov, Rev. Mod. Phys. **78**, 309 (2006).
- <sup>3</sup>M. Marklund, P.K. Shukla, Rev. Mod. Phys. **78**, 591 (2006).
- <sup>4</sup>A. Di Piazza, C. Muller, K. Z. Hatsagortsyan, C. H. Keitel, Rev. Mod. Phys. **84**, 1177 (2012).
- <sup>5</sup>E. Nerush, I. Kostyukov Phys. Rev. E **75**, 057401 (2007).
- <sup>6</sup>C. P. Ridgers, C. S. Brady, R. Ducloux, J. G. Kirk, K. Bennett, T. D. Arber, A. P. L. Robinson, A. R. Bell, Phys. Rev. Lett. **108**, 165006 (2012).
- <sup>7</sup>J. G. Kirk, A. R. Bell, C. P. Ridgers, Plasma Phys. Control. Fusion **55**, 095016 (2013).
- <sup>8</sup>A. V. Bashinov and A. V. Kim, Phys. Plasmas **20**, 113111 (2013).
- <sup>9</sup>C. S. Brady, C. P. Ridgers, T. D. Arber, A. R. Bell, Phys. Plasmas **21**, 033108 (2014).
- <sup>10</sup>E. N. Nerush, I. Yu. Kostyukov, L. Ji, A. Pukhov, Phys. Plasmas **21**, 013109 (2014).
- <sup>11</sup>E. N. Nerush, I. Yu. Kostyukov, Plasma Phys. Control. Fusion **57**, 035007 (2015).
- <sup>12</sup>A. R. Bell and J. G. Kirk, Phys. Rev. Lett. **101** 200403 (2008).
- <sup>13</sup>A. M. Fedotov *et al.* Phys. Rev. Lett. **105** 080402 (2010).
- <sup>14</sup>E. N. Nerush, I. Yu. Kostyukov, A. M. Fedotov, N. B. Narozhny, N. V. Elkina, and H. Ruhl, Phys. Rev. Lett. **106**, 035001 (2011).
- <sup>15</sup>S. S. Bulanov, C. B. Schroeder, E. Esarey, W. P. Leemans, Phys. Rev. A **87**, 062110 (2013).
- <sup>16</sup>V. F. Bashmakov, E. N. Nerush, I. Yu. Kostyukov, A. M. Fedotov, N. B. Narozhny, Phys. Plasmas **21**, 013105 (2014).
- <sup>17</sup>E. G. Gelfer, A. A. Mironov, A. M. Fedotov, V. F. Bashmakov, E. N. Nerush, I. Yu. Kostyukov, N. B. Narozhny, Physical Review A **92**, 022113 (2015).
- <sup>18</sup>M. Jirka, O. Klimo, S. V. Bulanov, T. Zh. Esirkepov, E. Gelfer, S. S. Bulanov, S. Weber, and G. Korn, Phys. Rev. E **93**, 023207 (2016).
- <sup>19</sup>M. Vranic, J. L. Martins, R. A. Fonseca, L. O. Silva, Laser absorption via QED cascades in counter propagating laser pulses, arXiv:1512.05174.
- <sup>20</sup>G. Lehmann, and K. H. Spatschek, Phys. Rev. E **85**, 056412 (2012).
- <sup>21</sup>L. L. Ji, A. Pukhov, I. Yu. Kostyukov, B. F. Shen, K. U. Akli, Phys. Rev. Lett. **112**, 145003 (2014).
- <sup>22</sup>A. Gonoskov, A. Bashinov, I. Gonoskov, C. Harvey, A. Ilderton, A. Kim, M. Marklund, G. Mourou, and A. Sergeev, Phys. Rev. Lett. **113**, 014801 (2014).
- <sup>23</sup>A. M. Fedotov, N. V. Elkina, E. G. Gelfer, N. B. Narozhny, and H. Ruhl, Phys. Rev. A **90**, 053847 (2014).
- <sup>24</sup>J. G. Kirk, Radiative trapping in intense laser beams, arXiv:1605.00822.
- <sup>25</sup>W. L. Kruer, E. J. Valeo, and K. G. Estabrook, Phys. Rev. Lett. **35**, 1076 (1975).
- <sup>26</sup>S. C. Wilks, W. L. Kruer, M. Tabak and A. B. Langdon, Phys. Rev. Lett. **69**, 1383 (1992).

- <sup>27</sup>T. Schlegel, N. Naumova, V. T. Tikhonchuk, C. Labaune, I. V. Sokolov, G. Mourou, Phys. Plasmas **16**, 083103 (2009).
- <sup>28</sup>A. P. L. Robinson, P. Gibbon, M. Zepf, S. Kar, R. G. Evans and C. Bellei, Plasma Phys. Control. Fusion **51**,024004 (2009).
- <sup>29</sup>R. Capdessus and P. McKenna, Phys. Rev. E **91**, 053105 (2015).
- <sup>30</sup>V. N. Baier, V. M. Katkov, and V. M. Strakhovenko, *Electromagnetic Processes at High Energies in Oriented Single Crystals* (Singapore, World Scientific 1998).
- <sup>31</sup>V. B. Berestetskii, E. M. Lifshits, and L. P. Pitaevskii, *Quantum Electrodynamics* (Pergamon Press, New York, 1982).
- <sup>32</sup>L. D. Landau, E. M. Lifshits, *The Classical Theory of Fields* (Pergamon, New York, 1982).
- <sup>33</sup>R. Duclous, J. G. Kirk and A. R. Bell, Plasma Phys. Control. Fusion **53**, 015009 (2011).
- <sup>34</sup>Ya. B. Zel'dovich, Sov. Phys. Usp. **18**, 97 (1975).
- <sup>35</sup>S. V. Bulanov, T. Zh. Esirkepov, M. Kando, J. K. Koga, S. S. Bulanov, Phys. Rev. E **84**, 056605 (2011).
- <sup>36</sup>N. V. Elkina, A. M. Fedotov, I. Yu. Kostyukov, M. V. Legkov, N. B. Narozhny, E. N. Nerush, and H. Ruhl, Phys. Rev. ST Accel. Beams **14**, 054401 (2011).
- <sup>37</sup>T. Grismayer, M. Vranic, J. L. Martins, R. A. Fonseca, L. O. Silva, Seeded QED cascades in counter propagating laser pulses, arXiv:1511.07503.
- <sup>38</sup>T. Z. Esirkepov, S. S. Bulanov, J. K. Koga, M. Kando, K. Kondo, N. N. Rosanov, G. Korn, and S. V. Bulanov, Physics Letters A **379** 2044 (2015).